INITIATION OF MATRIX CRACKING IN WOVEN CERAMIC MATRIX COMPOSITES

Mádhwapati Prabhakar Rao, Michael Pantiuk and Panos G. Charalambides
Department of Mechanical Engineering, University of Maryland Baltimore County
1000, Hilltop Circle
Baltimore
MD 21250

ABSTRACT

In this study, we employ detailed 3D finite element models of complex plain and satin weave ceramic matrix composites to address the problem of initiation of matrix cracking. Fundamental 3D elasticity boundary value problems addressing the response of these materials under the combined effects of remote biaxial tension and pure shear loads coupled with residual thermal stresses are utilized as needed to characterize the matrix micro-stresses in the vicinity of large-scale macroscopic voids. The combined stress fields are then used to determine the effects of remotely applied in-plane loads and thermal temperature gradients on the initiation of matrix cracking in the region of high stress concentrations. Selective comparison of model results with available experimental data are discussed. Extensive parametric studies have been carried out and robust failure loci predictive of the "first" matrix cracking events have been developed. The availability of such failure envelopes for woven CMCs offers for the first time a design tool for the use of such advanced systems in engineering applications.

INTRODUCTION

Woven fabric composites can be engineered to provide high strength, stiffness and toughness in comparison with conventional monolithic materials for a wide variety of land, sea and space based applications. However these materials are characterized by a complex three-dimensional geometry and intricate microstructures [1]. As such robust solution techniques capable of predicting the micro-stress elastic fields are needed in the quantification of life limiting failures in these systems.

When woven CMCs are loaded in-plane, micro-failure events such as matrix microcracking, fiber debonding, fiber bridging, frictional fiber pull-out and fiber tow delamination have been shown to occur [2, 3]. Overall woven CMCs are known to exhibit a nonlinear stress-strain curve characterized by a graceful ultimate failure [3]. Under the influence of high temperature gradients, the apparent strength of woven CMCs has been shown to decrease mainly due to residual stresses induced by thermal expansion mismatch of the fiber and matrix materials [4]. Most applications with these material systems are likely to be designed using the "first knee" of the general nonlinear stress-strain curve as the stress design limit. This "first knee" has been shown to coincide with the "first matrix cracking" stress identified as the proportional limit of the woven composite material [5].

From the standpoint of engineering design, the proportional limit stress of woven CMCs

is a parameter of critical importance. Experimentally established tensile stress-strain curves for a SiC/SiC plain weave system obtained by Williams International, Inc. and CCI, Inc. are shown in Figure 1 which clearly indicate that the proportional limit stress of woven CMCs indeed decreases with increasing temperature. Therefore, the objective of this work is to develop broad failure loci for a plain weave C/SiC system subjected to a combination of in-plane mechanical loads and thermal temperature gradients and in which the fibers and matrix are thermally different.

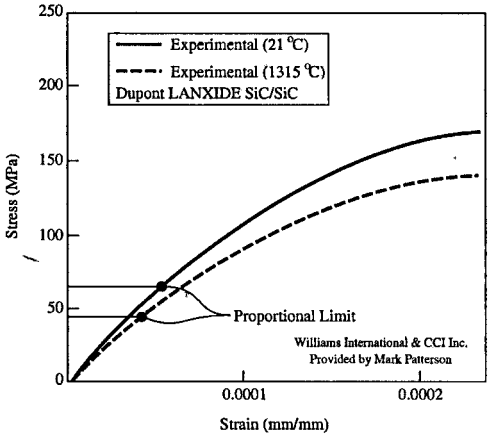

Figure 1: Experimentally established stress-strain curves for a DuPont Lanxide plain weave SiC/SiC composite. Data reported by Patterson [5, 6].

FINITE ELEMENT MODELING

In this work we model the mechanical response of complex woven CMCs employing the finite element method. Detailed three-dimensional (3D) finite element models of the symmetric unit-cells of woven CMCs are developed using 3D 8-noded isoparametric brick elements, consistent with studies reported elsewhere [7, 8, 9]. The fiber tows are modeled as transversely isotropic material entities with directional effective properties while the matrix material is modeled as an isotropic medium with dispersed porosity. Symmetry boundary conditions are enforced on the woven unit-cells as required to simulate in-plane mechanical loads and thermal expansion effects.

Geometric Modeling

An improved binary sub-cell method was developed to model the geometry of Four Harness (4HS), Five Harness (5HS) and Eight Harness (8HS) satin weave composites on the lines of the methodology suggested by Hewitt et. al. [10] without sacrificing the details about the cross-sectional shapes and undulating profiles of the fiber tows. However, this

study represents a marked improvement over the previous models since discrete large matrix voids as well as dispersed matrix porosity are incorporated into hierarchical models capable of predicting the macroscopic response while maintaining the integrity of the microstructure. These hierarchical models can now be used to predict micro-stress concentration sites and induced damage associated with the non-linear branch of the stress-strain curves [5, 11]. The modeling of the Plain Weave geometry follows the techniques described in [7]. Figure 2 shows a library of the finite element models of the symmetric unit-cells of the woven composites modeled as part of an ongoing research effort.

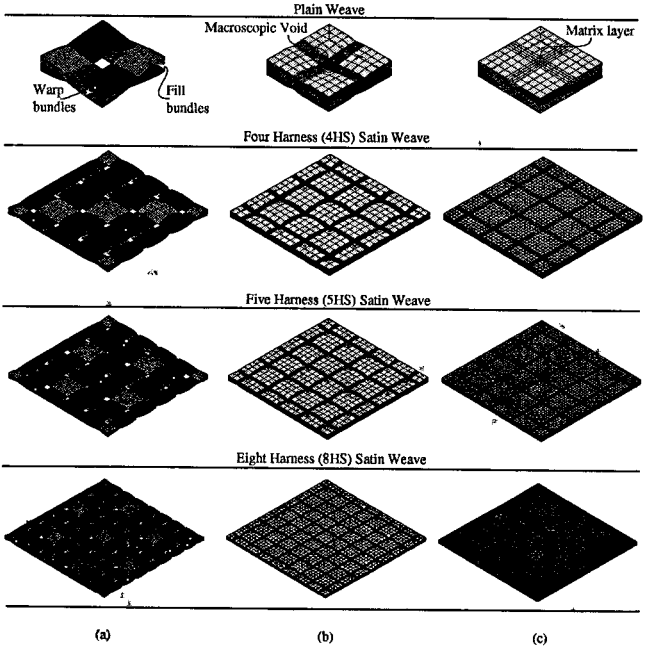

Figure 2: Geometric finite element models of the symmetric unit-cells of various woven composites. (a) Fiber bundle architecture of plain and satin weave composites. (b) Ceramic matrix layer deposited on woven fibers via the Chemical Vapor Infiltration (CVI) technique. (c) Polymer matrix layer deposited on woven fibers.

The analysis presented as part of this work was performed on a plain weave C/SiC system with non-dimensional spatial variables listed in Table I . The half-period of fiber tow undulation a was chosen as the characteristic spatial dimension to normalize the spatial variables. This approach is consistent with the non-dimensionalization procedure developed in [7, 8]. A representative finite element mesh made with the geometric input parameters of

Table I is shown in Figure 3. The actual mesh used in the parametric studies was discretized with 17920 3D 8-noded isoparamteric brick elements. The model consisted of 20611 finite element nodes resulting in a total of 61833 degrees of freedom. The physical properties of the plain weave C/SiC system modeled in this work are given in Table II.

Table I: Microstructural Geometry Parameters.

Parameter	Description	Value
$\hat{a}$	a/a	1.0
$\hat{b}$	b/a	0.10
$\hat{g}$	g/a	0.15
$\hat{t}$	t/a	0.04
$\hat{h}$	h/a	$2\hat{b}$

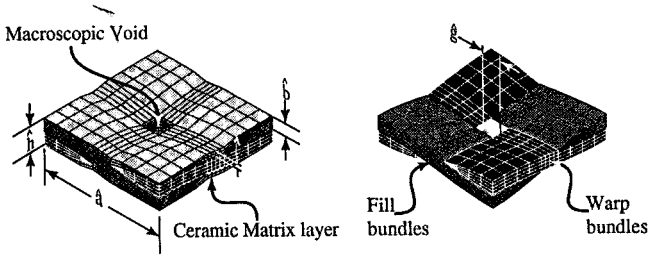

Figure 3: Finite element mesh of the plain weave C/SiC system studied in this work.

Material Properties

The microstructure of woven CMCs is hierarchical as depicted in the micrograph of Figure 4. The finite element models designed as part of this study account for such heterogeneity in the microstructure employing the robust four-step homogenization scheme developed by Kuhn and Charalambides [8]. A graphical description of the four-step homogenization procedure is shown in Figure 5. The homogenization scheme is applied to obtain the effective properties of the fiber tow which are then used in conjunction with proper material property rotation as input to the global finite element model for characterizing the effective macroscopic response of woven composites.

In Step # 1 of the homogenization scheme (see Figure 5 (b)), the fiber and and fiber coating are homogenized into an effective orthotropic fiber employing the Composite Cylinders Assemblage model. During Step # 2 of this homogenization scheme (see Figure 5 (c)), the bundle matrix and bundle porosity are combined into an effective isotropic bundle matrix by employing the porosity micromechanics model. Step # 3 of the homogenization scheme,

Table II: Physical properties of the plain weave C/SiC system studied. These properties were provided by Ceramic Composites, Inc.

Entity	Description
Fiber	Toray T-300 1K tow carbon fiber
Matrix	SiC
Tensile Strength	$\simeq$ 300 MPa
Fiber Content	40% by volume
Process	Chemical Vapor Infiltration (CVI)
Modulus	Not Available
Composite Proportional Limit	80 MPa (Tensile)

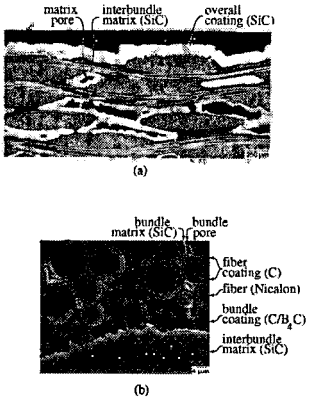

Figure 4: Micrographs of a SiC/SiC plain weave composite. (a) Sectional view of the laminate clearly showing dispersed matrix porosity. (b) Close-up view of a single fiber bundle cross-section illustrating a hierarchical microstructure.

once again employs the CCA model to homogenize the effective fibers and effective matrix into an orthotropic fiber tow (see Figure 5 (d)). The final step (see Figure 5 (e)) of this homogenization scheme, converts the effective orthotropic fiber and the bundle coating into an orthotropic material entity (fiber tow) with coating using the CCA model. The matrix between the fiber tows (inter-bundle matrix) and the associated porosity are homogenized into an effective isotropic matrix using the porosity micromechanics model.

The material micro-constituents viz., the fibers, fiber coating, bundle matrix, bundle coating, bundle porosity, inter-bundle matrix and inter-bundle matrix porosity are represented through the volume fractions C_f, C_{fc}, C_{bm}, C_{bc}, C_{bp}, C_m and C_{mp} respectively and

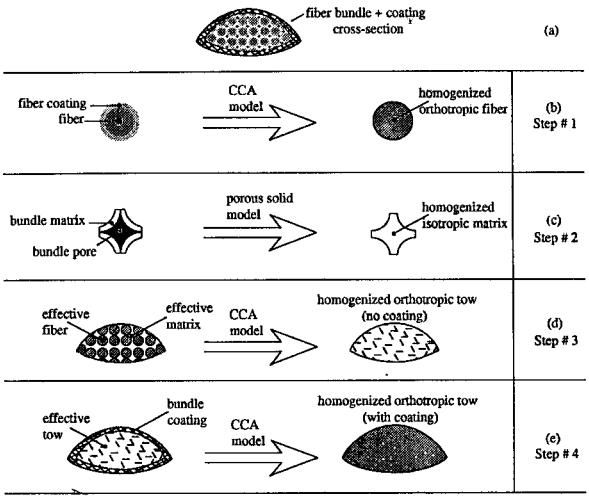

Figure 5: The four-step homogenization procedure developed by Kuhn and Charalambides [8].

are subject to the following consistency conditions:

$$\begin{aligned} C_f + C_{fc} + C_{bm} + C_{bc} + C_{bp} &= 1 \\ C_m + C_{mp} &= 1 \end{aligned} \tag{1}$$

Table III: Microstructural Material Parameters.

	Elastic Modulus	Poisson's Ratio	Shear Modulus	CTE	Volume Fraction
Fiber	$\hat{E}_f = 0.8$	$\hat{\nu}_f = 0.43$	$\hat{G}_f = 0.28$	$\hat{\alpha}_f = 0.3$	$C_f = 0.75$
Fiber Coating	$\hat{E}_{fc} = 0.125$	$\hat{\nu}_{fc} = 0.3$	$\hat{G}_{fc} = 0.05$	$\hat{\alpha}_{fc} = 1.0$	$C_{fc} = 0.05$
Bundle Matrix	$\hat{E}_{bm} = 1.0$	$\hat{\nu}_{bm} = 0.3$	$\hat{G}_{bm} = 0.385$	$\hat{\alpha}_{bm} = 1.0$	$C_{bm} = 0.14$
Bundle Coating	$\hat{E}_{bc} = 0.25$	$\hat{\nu}_{bc} = 0.25$	$\hat{G}_{bc} = 0.1$	$\hat{\alpha}_{bc} = 1.0$	$C_{bc} = 0.05$
Bundle Porosity	–	–	–	–	$C_{bp} = 0.01$
Inter-Bundle Matrix	$\hat{E}_m = 1.0$	$\hat{\nu}_m = 0.3$	$\hat{G}_m = 0.385$	$\hat{\alpha}_m = 1.0$	$C_m = 0.9$
Matrix Porosity	–	–	–	–	$C_{mp} = 0.1$

All calculations are performed in a non-dimensional environment consistent with [8, 12]. The inter-bundle matrix is chosen as the characteristic material. Table III describes the

normalized material property data input to the finite element model. In Table III the "hat" notation ($\hat{()}$) on a modulus signifies that the property has been normalized with respect to the matrix elastic modulus E_m, whereas the "hat" notation ($\hat{()}$) on a Coefficient of Thermal Expansion (CTE) value implies that it has been normalized with respect to the matrix CTE α_m. The material micro-constituent input data presented in Table III is employed to homogenize the fiber tow and inter-bundle matrix material. The effective properties of the fiber tows and matrix material computed using the homogenization scheme developed by Kuhn and Charalambides [8] are shown in Table IV.

Table IV: Meso-scopic Output.

Effective Tow	Effective Matrix
$\hat{E}_{11} = 0.7591$	$\hat{E}_{\overline{m}} = 0.810$
$\hat{E}^l_{22} = 0.636$	$\hat{G}_{\overline{m}} = 0.314$
$\hat{G}_{12} = 0.239$	$\hat{\nu}_{\overline{m}} = 0.288$
$\hat{G}_{23} = 0.239$	$\hat{\alpha}_{\overline{m}} = 1.0$
$\hat{\nu}_{12} = 0.397$	
$\hat{\nu}^l_{23} = 0.379$	
$\hat{\alpha}_{11} = 0.4395$	
$\hat{\alpha}_{22} = 0.4263$	

The effective tow and matrix properties presented in Table IV are used to compute the transformed reduced stiffness matrix $[\overline{Q}]$ and input as the Material Property Matrix $[D]$ in the finite element model [11].

Boundary Conditions

The symmetry boundary conditions which are imposed on the woven unit-cells to simulate pure remote tension and shear loading are derived from the work of Kuhn and Charalambides [8, 12]. However, the boundary conditions for free thermal expansion are different as explained in Figure 6. As shown in Figure 6 (b), to simulate free thermal expansion, symmetry boundary conditions are imposed on the lateral faces at $\hat{x} = -\hat{a}/2$ and $\hat{y} = -\hat{a}/2$. In particular on the face at $\hat{x} = -\hat{a}/2$, the displacement of all the nodes along the global $\hat{x}$-direction is set equal to zero, i.e. $\hat{u}_x = 0$, whereas on the face of the woven unit-cell corresponding to $\hat{y} = -\hat{a}/2$, the displacement of all nodes in the global $\hat{y}$-direction is set equal to zero, i.e. $\hat{u}_y = 0$. However, on the opposite faces corresponding to $\hat{x} = \hat{a}/2$ and $\hat{y} = \hat{a}/2$, we impose constraint conditions thereby ensuring the planarity of these faces before and after deformation (as dictated by symmetry). More specifically, we require that all the nodes on the face of the woven unit-cell corresponding to $\hat{x} = \hat{a}/2$ should move by the same amount along the global $\hat{x}$-direction, i.e. $\hat{u}_x = C$, whereas all the nodes on face of the woven unit-cell at $\hat{y} = \hat{a}/2$ are forced to move by an equal amount along the global $\hat{y}$-direction, i.e. $\hat{u}_y = C$.

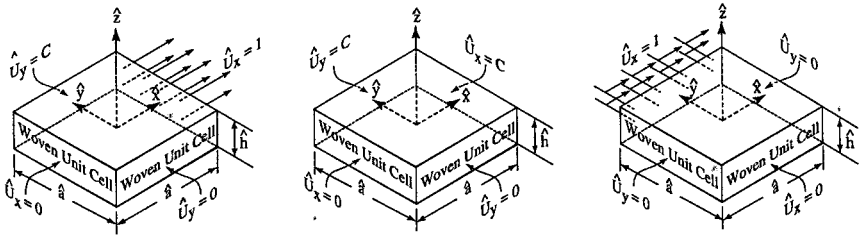

Figure 6: Schematic representation of the boundary conditions imposed on the woven unit-cells to simulate different loading conditions. Rigid body motions in the z-direction are constrained by enforcing zero displacements in the same direction at least at one node in the FE model.

MODEL FORMULATION

In-plane mechanical loads can either be represented through the stresses σ_{xx}^{∞}, σ_{yy}^{∞} and τ_{xy}^{∞} or via the spherical loading parameters, ω, ϕ and S. Figure 7 defines these parameters and also graphically illustrates the stress fields resulting from the four fundamental boundary value problems solved in order to develop failure loci aimed at assessing the strength of woven CMCs under combined mechanical and thermal loads.

The remotely applied in-plane mechanical loads can be related to the spherical loading parameters as:

$$\begin{aligned} \sigma_{xx}^{\infty} &= S cos\phi cos\omega \\ \sigma_{yy}^{\infty} &= S cos\phi sin\omega \\ \tau_{xy}^{\infty} &= S sin\phi \end{aligned} \tag{2}$$

It has been shown in previous studies [13, 14] that the total stress induced in the woven CMCs scales linearly with the remotely applied loads. Based on the principle of linear superposition, the total stress is given by:

$$\sigma_{ij}^{total} = \sigma_{ij}^{x} + \sigma_{ij}^{y} + \tau_{ij}^{xy} + \sigma_{ij}^{th} \tag{3}$$

where the ij-component of each individual stress is induced by the corresponding remotely applied mechanical or thermal load. For example, σ_{ij}^{x} is the ij-component of stress induced by σ_{xx}^{∞}. It can be shown that the total stress is related to the spherical loading parameters and induced non-dimensional stresses via a functional relationship of the form [5]:

$$\sigma_{ij}^{total} = S\hat{\Sigma}_{ij}^{total}\left(\omega, \phi, \beta, \hat{\sigma}_{ij}^{x}, \hat{\sigma}_{ij}^{y}, \hat{\tau}_{ij}^{xy}, \hat{\sigma}_{ij}^{th}\right) \tag{4}$$

where β is a loading proportionality constant measuring the ratio of thermal to mechanical

loads and is given by:

$$\beta = \frac{E_c \alpha_c \Delta T_c}{S} \tag{5}$$

In Equation 5 E_c, α_c and ΔT_c are the characteristic elastic modulus, Coefficient of Thermal Expansion (CTE) and characteristic temperature difference, while S is the magnitude of the proportional mechanical load measured in the units of stress.

Matrix Micro-Stresses

Figure 7 shows contour plots of stress induced in the plain weave C/SiC system due

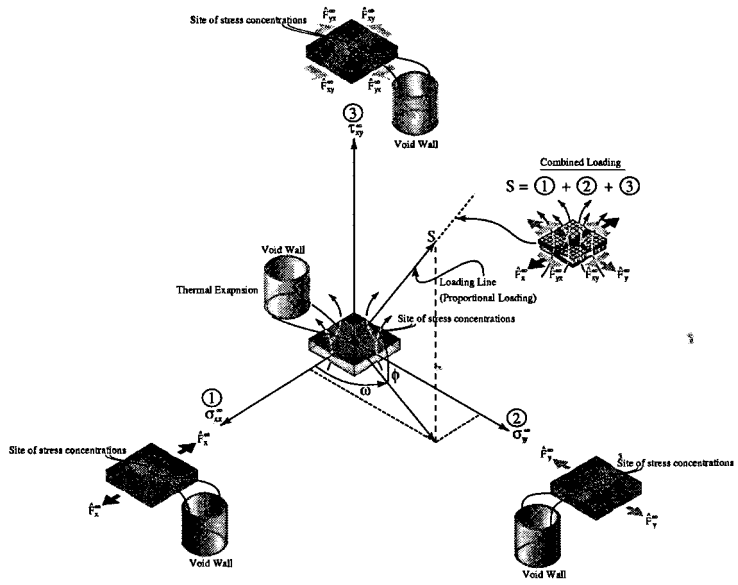

Figure 7: The induced matrix micro-stresses as a result of in-plane mechanical loads and free thermal expansion.

to in-plane mechanical loads and free thermal expansion. For the sake of clarity, a blow-up of stresses induced in the vicinity of the macroscopic void are shown adjacent to each contour plot. The average stresses in the void wall are calculated by first computing the stress at the center of each finite element belonging to the free surface adjacent to the void and then averaging the stresses in the z-direction, in the finite elements at the same angular distance θ from the center of the void. As a result, the induced stresses due to the action of mechanical tension along the x-direction are represented as shown in Figure 8. The $\hat{\sigma}_{xx}$ stress assumes maximum values at $\pm 90°$ from the center of the void. These profiles suggest that stress concentrations occur in the void along planes orthogonal to the direction of pull.

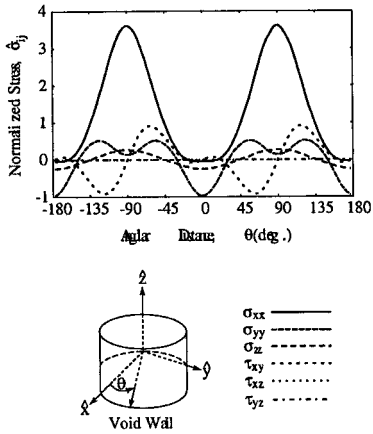

Figure 8: Profiles of induced matrix micro-stresses in the vicinity of the macroscopic void due to tension along the x-direction ($\omega = 0$, $\phi = 0°$).

The magnitudes of the stresses shown in Figure 8 suggest that the maximum induced non-dimensional $\hat{\sigma}_{xx}$ stress is of the order of about 3.5 times the remotely applied mechanical load. Similar results due to mechanical tension along the y-direction, pure remote xy-shear and thermal loads are presented elsewhere [15].

Overall the findings regarding the stress fields in woven CMCs are consistent with previous research efforts [5, 14]. In both works cited above, it was shown clearly that damage bands begin to emanate from the vicinity of macroscopic voids in woven CMCs. These damage bands were also shown to be the most likely sites of initiation of cracking in the matrix material. As such, the stress results obtained in the present work inspire confidence in the finite element model.

The total stress induced in the vicinity of the matrix void is calculated with the aid of Equation 4 for different values of β. The effects of β which at least theoretically can take on values from $-\infty$ to $+\infty$ are explored through extensive parametric studies reported elsewhere [15]. However, in this work we present only the results corresponding to two distinct values of β = -3 and +3. Since the characteristic material and the remotely applied proportional mechanical load (S) do not change, each individual value of β really measures the total stress induced in the matrix void at a unique characteristic temperature difference. More specifically, $\beta \longrightarrow -\infty$ captures the case of pure thermal loading wherein $\Delta T_c < 0$ whereas $\beta \longrightarrow +\infty$ implies pure thermal loading with $\Delta T_c > 0$. As shown in Figure 9, with $\beta = -3$, $\hat{\sigma}_{xx}^{max}|_{\theta=\pm 90°} = 5.0$ whereas with $\beta = +3$, $\hat{\sigma}_{xx}^{max}|_{\theta=\pm 90°} = 2.2$, implying that stress concentrations increase as $\beta \longrightarrow -\infty$ and vice verse.

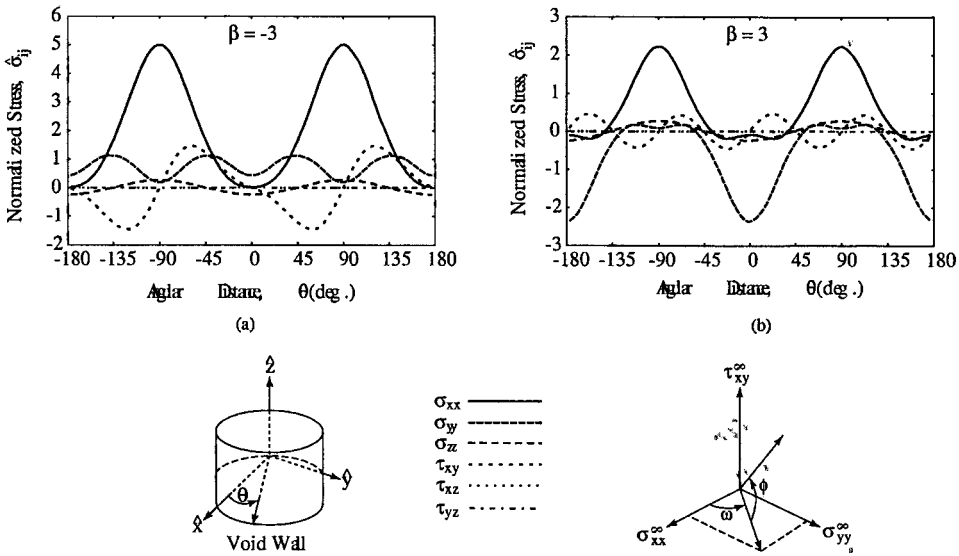

Figure 9: Profiles of total induced matrix micro-stresses in the vicinity of the macroscopic void, due to the combined effects of mechanical tension in the x-direction and thermal loading; i.e., $\omega = \phi = 0°$ and (a) $\beta = -3$ and (b) $\beta = +3$ with $\hat{\alpha}_f = \alpha_f/\alpha_m = 0.3$

Maximum Normal Stress Criterion

Using the functional relation of the total induced stress in the matrix void and the results shown in Figure 9, we will now develop a matrix failure function based on the normal stress criterion. According to normal stress criterion, a given material fails when the maximum normal stress at a point in the system reaches the ultimate tensile strength of the material. We can then write:

$$\sigma_{p1} = \sigma_{mf} \tag{6}$$

where σ_{p1} is the maximum normal stress and σ_{mf} is the matrix failure stress. We can obtain σ_{p1} as the biggest eigenvalue of the characteristic equation formed with the stress tensor given by σ_{ij}^{total}. In other words we solve the characteristic equation:

$$\left|\sigma_{ij}^{total} - \lambda\delta_{ij}\right| = 0 \tag{7}$$

where δ_{ij} is the Kronecker delta taking on a value of 1 if $i = j$ and 0 if $i \neq j$. The eigenvalues of σ_{ij}^{total} are obtained as the roots of the cubic characteristic equation of Equation 7 and σ_{p1} is assigned the value of the biggest eigenvalue as follows:

$$\sigma_{p1} = S\hat{\lambda}_1\left(\hat{\Sigma}_{ij}^{total}\right) \tag{8}$$

where $\hat{\lambda}_1$ is biggest eigenvalue of the normalized stress tensor given by $\hat{\Sigma}_{ij}^{total}$. Normalizing Equation 8 with the proportional mechanical load S and invoking the normal stress criterion Equation 6, we have a functional form of matrix failure given by:

$$\frac{\sigma_{mf}}{S} = \Omega_1 \left(\omega, \phi, \beta, \hat{\sigma}_{ij}^{x}, \hat{\sigma}_{ij}^{y}, \hat{\tau}_{ij}^{xy}, \hat{\sigma}_{ij}^{th}\right) \tag{9}$$

where the arguments of Ω_1 have the same meaning as explained in Equation 4.

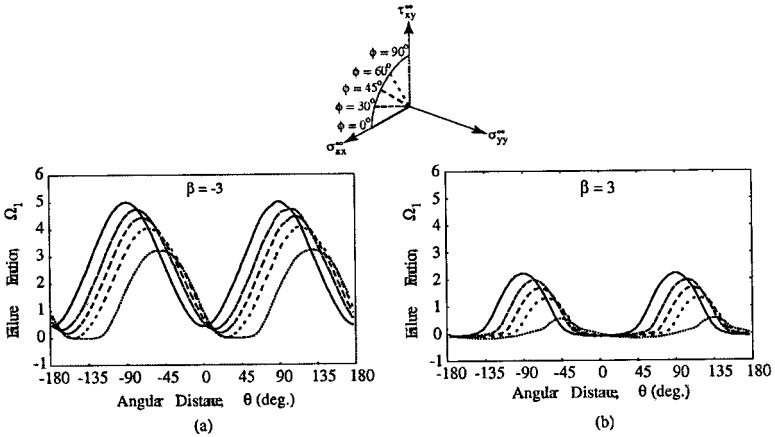

Figure 10: Profiles of the failure function based on the normal stress criterion. Combined effects of remote in-plane mechanical tension along the x-direction ($\omega = \phi = 0°$) and (a) $\beta = -3$ and (b) $\beta = +3$ with $\hat{\alpha}_f = \alpha_f/\alpha_m = 0.3$

Figure 10, reports on the effect of ω and β on Ω_1. To be consistent with the results presented for $\hat{\sigma}_{ij}^{total}$ in Figure 9, we present here results obtained for Ω_1 with β = -3 and +3 combined with mechanical loading in the x-direction ($\omega = 0°$). The five curves in both Figure 10 (a) and (b) correspond to increasing amounts of remotely applied in-plane mechanical shear load as measured via the spherical loading parameter ϕ. As expected, the failure function Ω_1 takes on maximum values when $\phi = 0°$ corresponding to zero in-plane shear load, regardless of the value of β. Another interesting feature represented by the results in Figure 10 is that the failure function Ω_1 takes on maximum values at $\pm 90°$ corresponding to $\phi = 0°$ and thereafter the magnitude of Ω_1 decreases with increasing shear load. Also it is worth noting that $|\Omega_1^{max}(\beta)|_{\phi=90°} \simeq |\Omega_1^{max}(\beta)|_{\phi=0°}/2$. These profiles of Ω_1 in Figure 10 suggest that failure is most likely to initiate at "equatorial" planes from the center of the matrix void regardless of the value of either β or ϕ.

Matrix Failure Loci

In order to further understand the effects of applied mechanical loads and temperature

gradients on the matrix failure stress, we developed matrix failure loci for the current plain weave C/SiC system being studied. The proportional loading vector $S = \sigma_{xx}^{\infty}\hat{i} + \sigma_{yy}^{\infty}\hat{j} + \tau_{xy}^{\infty}\hat{k}$ was employed along with the loading proportionality constant β to develop profiles of the failure function Ω_1 as shown in Figure 10. The maxima $\Omega_1^{max}(\beta)$ corresponding to Ω_1 was then used to develop a failure point in the normalized $\hat{\sigma}_{xx}^{\infty} - \hat{\tau}_{xy}^{\infty}$ space, for different combinations of ω and ϕ. Therefore, for a given remotely applied mechanical load controlled by the spherical loading parameters ω and ϕ, the matrix would fail in accordance with the normal stress criterion if:

$$\frac{\sigma_{xx}^{\infty}}{\sigma_{mf}} > \frac{cos\phi cos\omega}{\Omega_1^{max}(\beta)} \qquad \frac{\tau_{xy}^{\infty}}{\sigma_{mf}} > \frac{sin\phi}{\Omega_1^{max}(\beta)} \tag{10}$$

where $\Omega_1^{max}(\beta)$ implies that the maxima exhibited by Ω_1 is a function of the loading proportionality constant β. The matrix failure loci developed using this approach are shown in Figure 11.

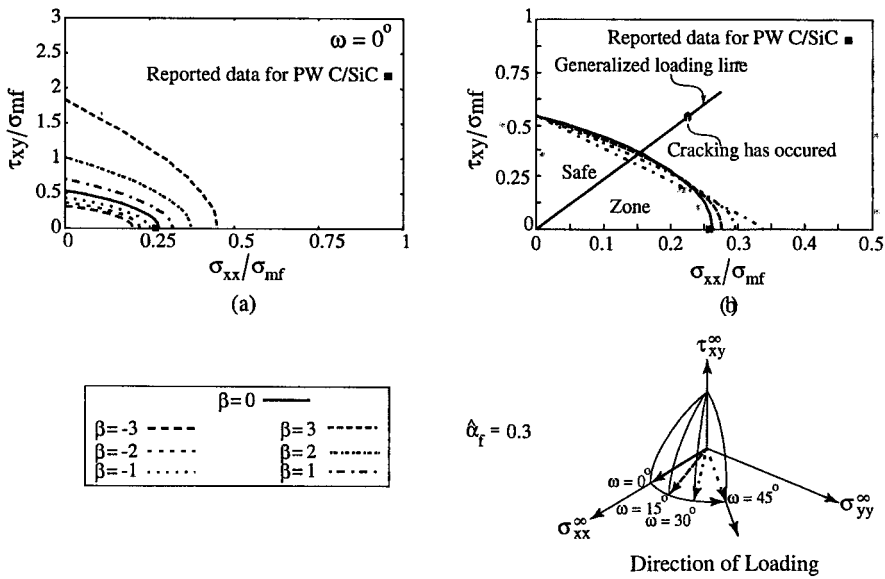

Figure 11: Profiles of the matrix failure loci for a plain weave C/SiC system based on the normal stress criterion.

Figure 11 (a) shows predicted failure for the plain weave C/SiC system under the combined action of remote in-plane mechanical tension in the x-direction and increasing amounts

of remote in-plane xy-shear along with thermal loading. It should be noted that when $\omega = 0°$, $\sigma^{\infty}_{yy} = 0$ and when $\omega = 45°$, $\sigma^{\infty}_{xx} = \sigma^{\infty}_{yy}$. In the absence of any temperature gradient ($\beta = 0$), the failure loci corresponding to increasing amounts of biaxial tension are shown in Figure 11 (b). The trends in the normalized failure loci shown in both Figure 11 (a) and (b) indicate that initiation of matrix cracking requires higher applied pure shear loads in comparison to pure tension loads for any given β, which gives rise to elliptical failure loci. In fact, from the results presented in Figure 11 it is clear that it takes about one-half of the remotely applied shear load to initiate matrix cracking in pure tension.

The experimentally established proportional limit data used to compare model predictions were provided by [6] (see Table II). When this data was normalized with respect to the SiC matrix failure stress of $\sigma_{mf} \simeq 300$MPa (also given in Table II) and superimposed on the failure loci, an excellent agreement between model predictions and experimental data was achieved for the case when $\omega = \phi = 0°$ (pure remote tension) and $\beta = 0$ (no thermal temperature gradients) as shown in Figure 11 (b).

It is also evident from Figure 11 that as $\beta \longrightarrow -\infty$, matrix cracking is predicted to initiate at lower remotely applied mechanical loads. This result implies that at higher temperature changes (ΔT), the strength of woven CMCs decreases due to significantly increased amounts of thermal stresses owing to the large mismatch in the CTEs of the fibers and matrix material.

CONCLUSIONS

A robust modeling framework for assessing the strength of woven CMCs under remotely applied in-plane mechanical loads and thermal temperature gradients has been developed. The detailed geometry models of woven CMCs employed in this work capture the local stress distribution around the vicinity of macroscopic matrix voids very accurately. The stress concentrations around these matrix voids were shown to be 3 to 4 times greater (for $\beta = 0$) than the remotely applied mechanical loads. With increasing temperature changes the thermal stresses appear to play a greater role most likely leading to a degradation in the apparent high temperature first cracking strength of woven CMCs. The adopted modeling approach is robust and can be employed to assess the strength of satin weave CMCs such as the four harness, five harness and eight harness systems. However more substantive comparisons with experimentally established temperature sensitive failure data for woven CMCs are needed for model validation.

References

[1] B. N. Cox and G. Flanagan. Handbook of Analytical Methods for Textile Composites. Technical report, NASA, March 1997.

[2] J. Lamon, N. Lissart, C. Rechiniac, D.H. Roach, and J.M. Jouin. Micromechanical and Statistical Approach to the Behavior of CMCs. *Ceramic Engineering Science Proceedings*, 14:1115–1124, 1993.

[3] X. Aubard, J. Lamon, and O. Allix. Model of the Nonlinear Mechanical Behavior of 2D SiC-SiC Chemical Vapor Infiltration Composites. *Journal of the American Ceramic Society*, 77(8):2118–2126, 1994.

[4] R. N. Singh. Fracture and Crack Growth in Ceramic Matrix Composites at High Temperatures. *Presented at the 106th Annual Meeting & Exposition of the American Ceramic Society, Indianapolis, IN.*, 2004.

[5] S. I. Haan. *Modeling of the Mechanical Response of Plain Weave Composites.* PhD thesis, The University of Maryland, 2000.

[6] M. C. L. Patterson. Private Communication. Advanced Ceramics Research, Tucson, AZ. Formerly at Ceramic Composites Inc., Millersville, MD.

[7] J. L. Kuhn and P. G. Charalambides. Modeling of Plain Weave Fabric Composite Geometry. *Journal of Composite Materials*, Vol. 33(3):188–220, 1999.

[8] J. L. Kuhn and P. G. Charalambides. Elastic Response of Porous Matrix Plain Weave Fabric Composites:Part I-Modeling. *Journal of Composite Materials*, Vol. 32(16):1426–1471, 1998.

[9] J. D. Whitcomb and X. Tang. Effective Moduli of Woven Composites. *Journal of Composite Materials*, 35(23):2127–2144, 2000.

[10] J. A. Hewitt, D. Brown, and R. B. Clarke. Computer Modelling of Woven Composite Materials. *Composites*, Vol. 26(2):143–140, 1995.

[11] J. L. Kuhn. *Mechanical Behavior of Woven Ceramic Matrix Composites.* PhD thesis, The University of Maryland, 1998.

[12] J. L. Kuhn and P. G. Charalambides. Elastic Response of Porous Matrix Plain Weave Fabric Composites:Part II-Results. *Journal of Composite Materials*, Vol. 32(16):1472–1507, 1998.

[13] J. L. Kuhn, S. I. Haan, and P. G. Charalambides. A Semi-Analytical Method for the Calculation of the Elastic Micro-Fields in PLain Weave Fabric Composites Subjected to In-Plane Loading. *Journal of Composite Materials*, Vol. 33(3):221–266, 1999.

[14] J. L. Kuhn, S. I. Haan, and P. G. Charalambides. Stress Induced Matrix Microcracking in Brittle Matrix PLain Weave Fabric Composites Under Uniaxial Tension. *Journal of Composite Materials*, Vol. 34(19):1640–1664, 2000.

[15] M. P. Rao, M. Pantiuk, and P.G. Charalambides. A Proportional Limit Model for Establishing the Failure Loci of Plain and Satin Weave Ceramic Matrix Composites. *In progress.*